Origami lattices with free-form surface ornaments

Janbaz, Shahram; Noordzij, Niels; Widyaratih, Dwisetya Safirna; Hagen, Kees; Fratila-Apachitei, LIdy; Zadpoor, Amir

DOI
10.1126/sciadv.aao1595

Publication date
2017

Document Version
Final published version

Published in
Science Advances

Citation (APA)
Janbaz, S., Noordzij, N., Widyaratih, D. S., Hagen, K., Fratila-Apachitei, LI., & Zadpoor, A. (2017). Origami lattices with free-form surface ornaments. *Science Advances*, *3*(11), Article eaao1595. https://doi.org/10.1126/sciadv.aao1595

MATERIALS SCIENCE

Origami lattices with free-form surface ornaments

**Shahram Janbaz,[1]* Niels Noordzij,[2] Dwisetya S. Widyaratih,[1] Cornelis W. Hagen,[2]
Lidy E. Fratila-Apachitei,[1] Amir A. Zadpoor[1]**

Lattice structures are used in the design of metamaterials to achieve unusual physical, mechanical, or biological properties. The properties of such metamaterials result from the topology of the lattice structures, which are usually three-dimensionally (3D) printed. To incorporate advanced functionalities into metamaterials, the surface of the lattice structures may need to be ornamented with functionality-inducing features, such as nanopatterns or electronic devices. Given our limited access to the internal surfaces of lattice structures, free-form ornamentation is currently impossible. We present lattice structures that are folded from initially flat states and show that they could bear arbitrarily complex surface ornaments at different scales. We identify three categories of space-filling polyhedra as the basic unit cells of the cellular structures and, for each of those, propose a folding pattern. We also demonstrate "sequential self-folding" of flat constructs to 3D lattices. Furthermore, we folded auxetic mechanical metamaterials from flat sheets and measured the deformation-driven change in their negative Poisson's ratio. Finally, we show how free-form 3D ornaments could be applied on the surface of flat sheets with nanometer resolution. Together, these folding patterns and experimental techniques present a unique platform for the fabrication of metamaterials with unprecedented combination of physical properties and surface-driven functionalities.

INTRODUCTION

Rational design of the small-scale topology is the primary way of achieving unusual physical properties in many types of optical (*1*–*3*), electromagnetic(*4*), acoustic (*5*), and mechanical (*6*) metamaterials. Lattice structures have been often used in these topological designs to develop, among others, ultralight yet ultrastiff materials (*7*), fluid-like solids (meta-fluids) (*8*), materials with ultrahigh energy absorption properties (*9*), auxetic materials (*10*), and materials that exhibit negative and adjustable thermal expansion (*11*). The fact that the porosity and, thus, mass transport properties (that is, permeability and diffusivity) of lattice structures could be easily adjusted is instrumental to certain application areas, such as regenerative medicine (*12*, *13*), where the nutrition and oxygenation of cells particularly at the early phases of tissue regenerations are dependent on diffusion. Modern three-dimensional (3D) printing techniques have enabled production of lattice structures with arbitrarily complex topologies and with increasing accuracies at the micro- (*14*) and nanoscales (*15*–*17*).

Multifunctional metamaterials often require incorporation of functionality-inducing surface features onto the surface of lattice structures. For example, very specific types of nanotopographical features (*18*–*21*) applied on the surface of tissue engineering scaffolds (*22*) regulate focal adhesion (*23*) and activate certain mechanotransductory pathways (*24*) that determine the stem cell fate. Nanotopographical features on the surface of metamaterials could also induce other types of functionalities, such as superhydrophilicity and superhydrophobicity (*25*–*27*), antireflective properties (*28*), and antibacterial behavior (*29*, *30*). Devices such as (printed) sensors and actuators could be also integrated onto the surface of metamaterials to create metamaterials with more advanced functionalities. Advanced micro- and nanopatterning techniques, such as electron beam nanolithography (*31*), nanoimprinting (*32*, *33*), dip-pen nanolithography (*33*, *34*), focused ion beam milling (*35*), and electron beam induced deposition (EBID) (*36*), allow for free-form patterning of surfaces. However, they generally work only on flat surfaces. Moreover, our access to the internal surface areas of 3D-printed lattice structures is very limited. Therefore, combining free-form surface ornaments with lattice topology is currently impossible. Inspired by the Japanese art of paper folding (origami), here we present an approach that allows for that combination. The lattice structures are folded from initially flat states that allow for free-form ornamentation and device incorporation using currently available techniques. Self-folding mechanisms have also been incorporated into the flat material to allow for self-folding into the final lattice shape.

From computational geometry, the foldability of a large number of simple polyhedral structures from flat pieces of paper is guaranteed (*37*). However, no such theorems exist for more complex polyhedral structures, such as polyhedral lattices. Moreover, the algorithms used for establishing the generality results are not practical because they are based on thin-paper assumptions and, thus, neglect the kinematic constraints that arise when folding real structures from sheets with finite thicknesses. In this work, we devised three folding patterns to fold various types of lattice structures from initially flat states (Fig. 1). Those folding patterns account for and accommodate the thickness of the flat structure and, hence, are relevant for practical applications.

RESULTS

Folding patterns

We considered lattices made by repeating a basic unit cell (with fixed shape and size) in different directions. Depending on the type of the repeating unit cell, a different folding pattern is needed. Unfolding the lattice to a fully flat state is the first step in devising the folding pattern. The lattice needs to be "sliced" along certain cutting planes to allow for separation and unfolding. Each of the three folding patterns devised here has different folding kinematics (Fig. 1 and figs. S1 to S3). The proposed categories are aimed to serve as intuitive frameworks, which guide the process of designing practical folding patterns for lattice structures of interest.

Category 1 includes the simplest types of unit cells with orthogonal fold lines (hinges), which generally require a single slice per lattice row

---

[1]Additive Manufacturing Laboratory, Department of Biomechanical Engineering, Delft University of Technology (TU Delft), Mekelweg 2, Delft 2628CD, Netherlands.
[2]Department of Imaging Physics, Faculty of Applied Physics, Delft University of Technology (TU Delft), Lorentzweg 1, Delft 2628CJ, Netherlands.
*Corresponding author. Email: s.janbaz@tudelft.nl

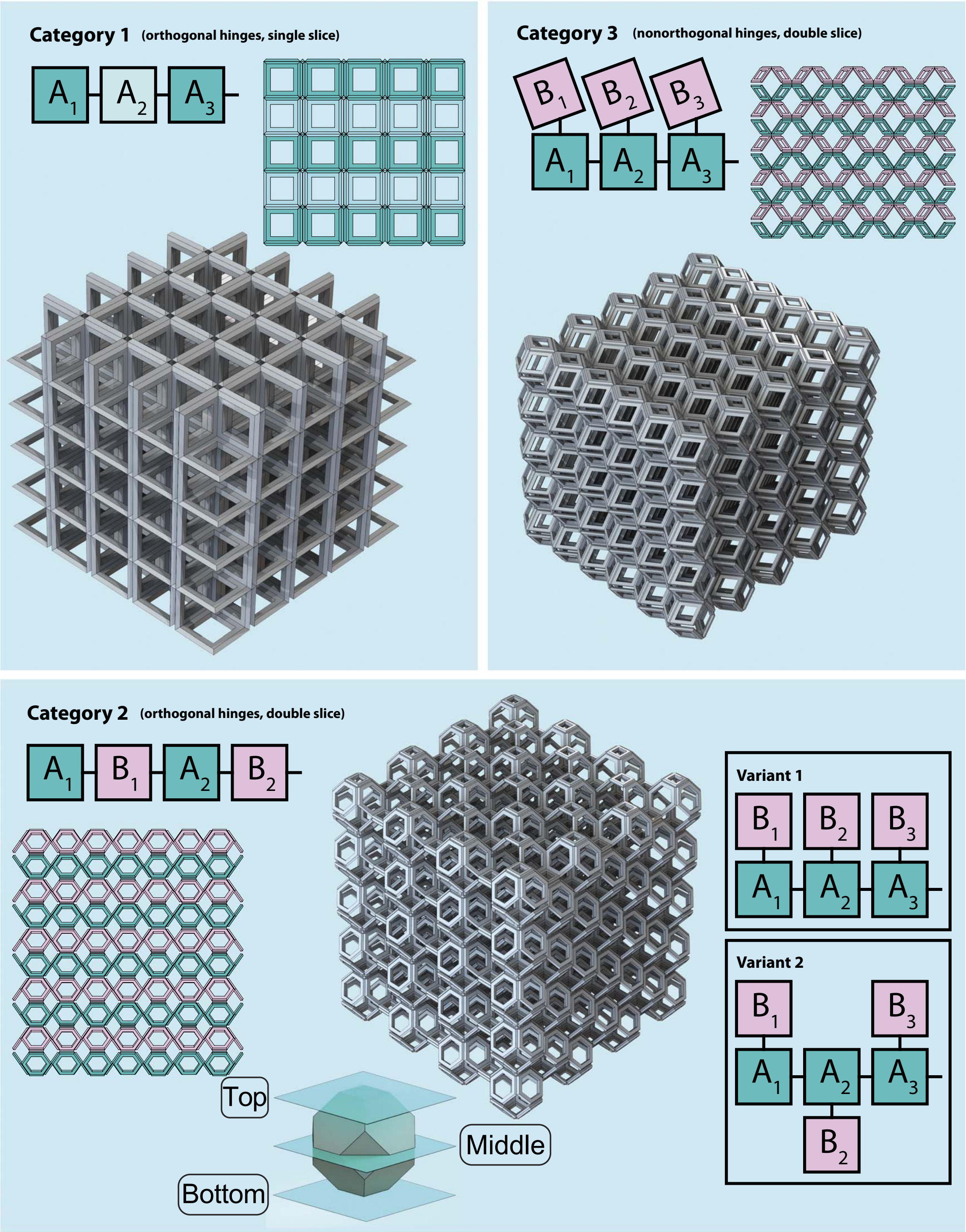

Fig. 1. Folding kinematics. (Category 1) To unfold category 1 lattices, every floor needs to be sliced at its boundary with the adjacent floor. Within this context, a floor is a row of the lattice structure. The unfolded floors (A_1, A_2,…) are connected in series. Here, a cubic lattice is illustrated as an example of category 1 lattices. Dark and light green denote the same type of folding pattern. (Category 2) The lattices belonging to this category need to be sliced at the middle of their floors as well as the boundary of the floors. The unfolded state of these lattices is made of a backbone that comprises every other half-floor (A_1, A_2,…) and the remaining half-floors (B_1, B_2,…) that branch out of the backbone. Therefore, green and pink colors denote folding patterns that face each other after folding. Alternative arrangements of the half-floors are possible, as shown in the two alternative variants. Here, a truncated octahedron lattice is depicted as an example of this category of foldable lattices. (Category 3) The unfolding of category 3 lattices is similar to that of category 2 lattices (a similar notation and color code are used), except that the positioning of the half-floors is not orthogonal anymore. A rhombic dodecahedron lattice is shown as an example of the foldable lattices from this category.

(floor; Fig. 1, category 1). The slicing planes are, thus, at the boundaries of the unit cells. Examples of space-filling polyhedra that belong in category 1 are cubic, truncated cube, and oblique rectangular prism. A representative layer (floor) has open faces at the top and closed faces at the bottom (top, middle, and bottom are visualized in an inset of Fig. 1). The thickness of the panels is incorporated by extruding the middle planes in both directions. The resulting panels are then chamfered at their edges to facilitate the folding process. In a thin-sheet design, the middle planes of the vertical faces would have overlapped with each other in the folded state. To accommodate the thickness in thick-sheet designs, the middle planes of the vertical faces were shifted by the thickness of one panel. Either a small connecting panel should then be positioned between two vertical panels or their thickness should be halved to allow for their folding (that is, 180° relative rotation). The vertical panels at the end of each floor (that is, monolayer) connect the panels of different floors with each other. In their unfolded states, the unfolded floors (A_1, A_2,… in Fig. 1) are connected to each other in series.

Category 2 covers more complex types of unit cells with orthogonal fold lines that require slicing along both top and bottom boundaries of the floors as well as through the middle of each floor (Fig. 1). Because half-floors overlap at their boundaries, the middle planes need to be shifted by the thickness of one panel. In their unfolded (that is, flat) state, the unfolded half-floors [A_1, A_2,… (green) and B_1, B_2,… (pink) in Fig. 1] are connected to each other in series. Alternatively, the unfolded half-floors could be connected to each other in several other ways (see variants 1 and 2 of category 2 in Fig. 2). Some of those variants are helpful

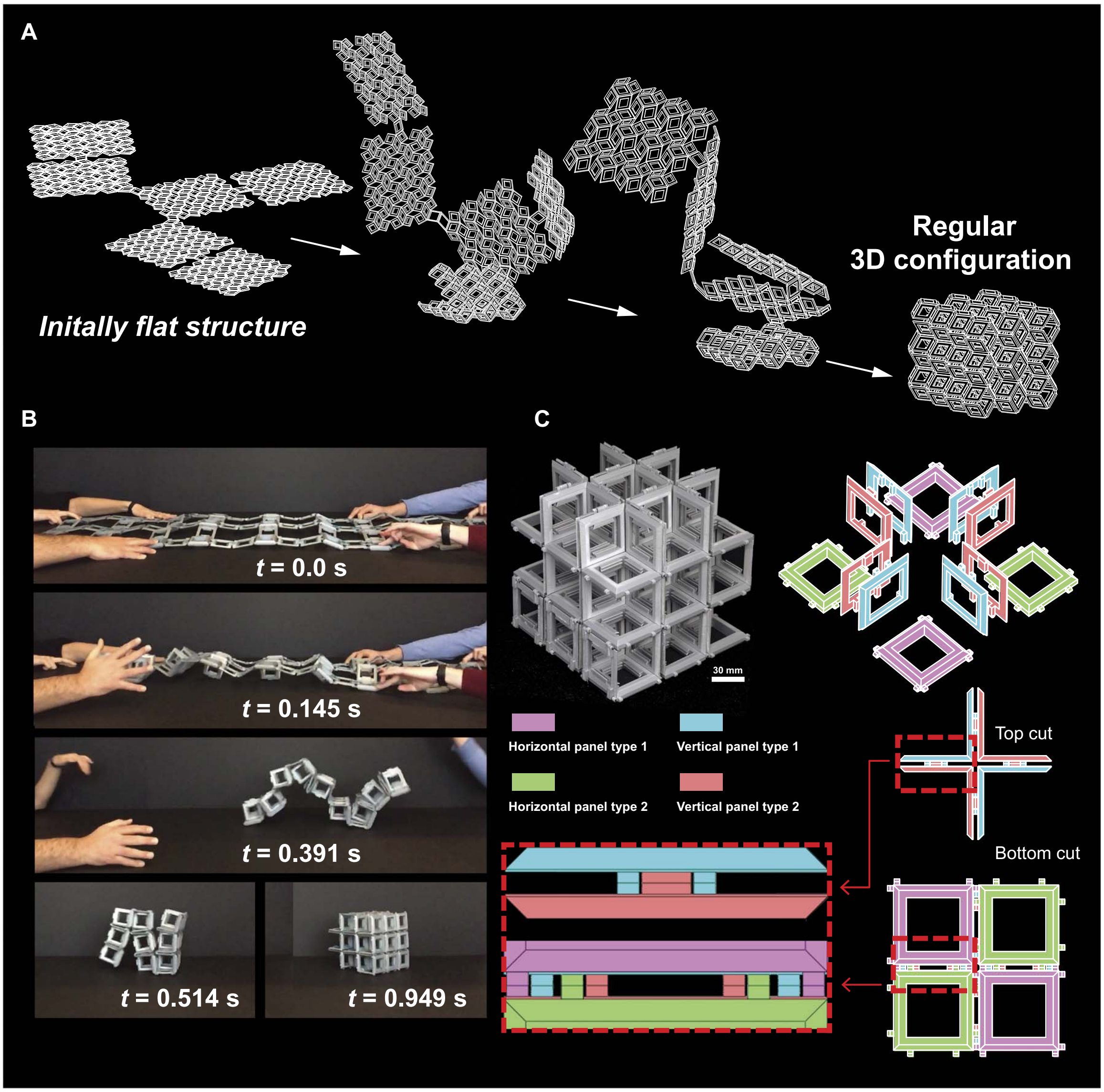

Fig. 2. (Self-)folding of origami lattices. (**A**) The folding sequences for a category 3 lattice (rhombic dodecahedron). Folding sequences of all other sample lattices of Fig. 1 can be seen in videos S1 to S3. (**B**) The time sequence of sequential self-folding in a three-story thick panel lattice. 3D-printed panels were hinged together using metal pins and a number of elastic rubber bands, and thus, the stored potential energy was used as a parameter for programming sequential self-folding. (**C**) The design of the self-folding lattice including the initial flat configuration and the final folded state. The hinges are designed to provide a confined space that locks the different floors after self-folding, thereby ensuring the integrity of the lattice and providing load-bearing capacity.

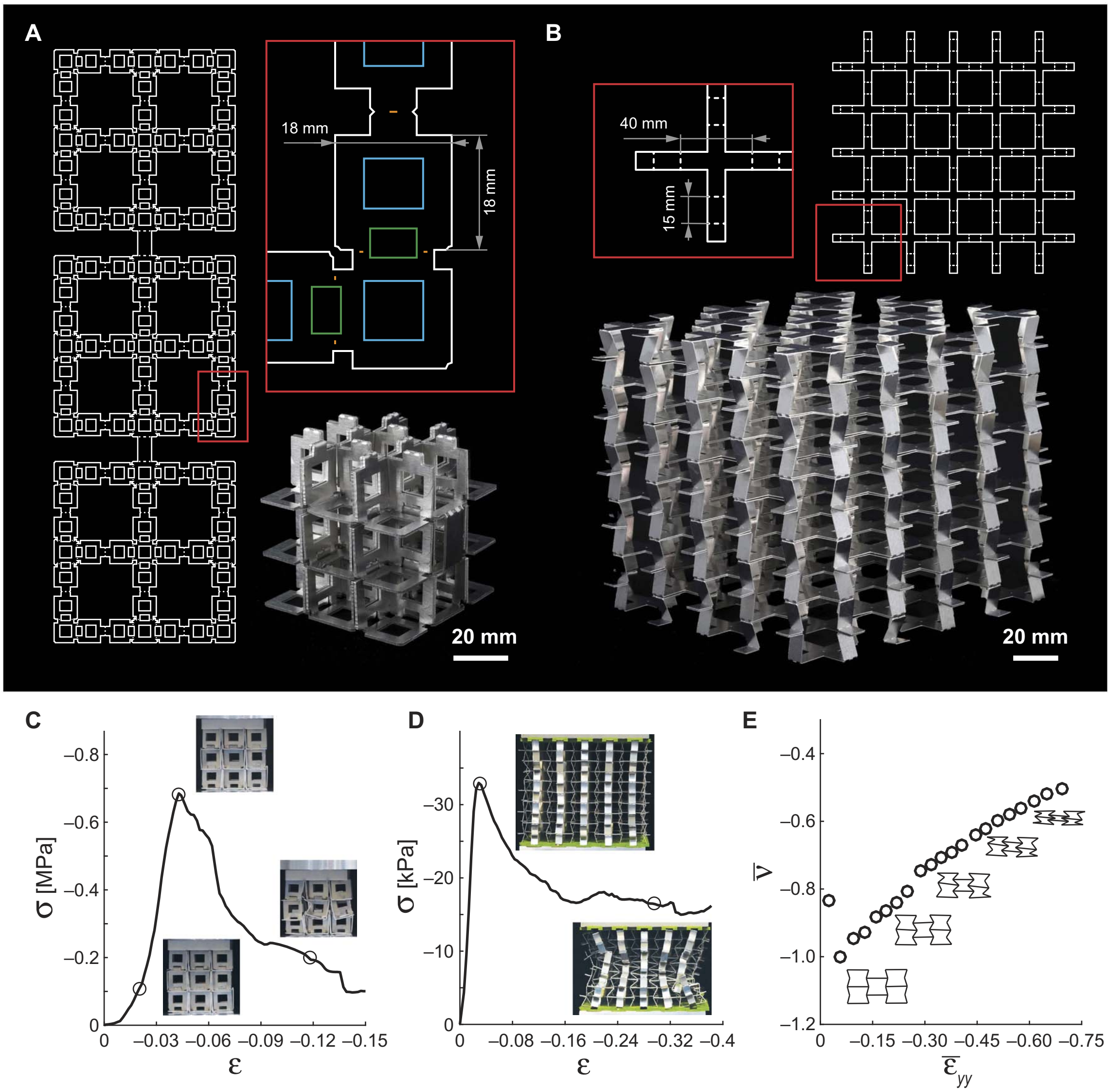

Fig. 3. Conventional and auxetic metallic origami lattices. (**A**) An aluminum cubic lattice structure comprising three unit cells in each direction. (**B**) Multilayer assembly of a reentrant lattice structure (a variant of truncated octahedron). (**C** and **D**) Compression stress-strain results for cubic and reentrant structures. (**E**) The evolution of the average Poisson's ratio with compressive strain, ε_{yy}, in the auxetic lattice. The evolution in the shape of the unit cells belonging to the ensemble that was used for calculating the Poisson's ratio is depicted as well.

when trying to circumvent the additional kinematic constraints faced with more complex designs of unit cells and to accommodate locking mechanisms. Examples of space-filling polyhedra that could be unfolded using this type of folding pattern are truncated octahedron and reentrant geometries.

Finally, category 3 covers space-filling polyhedra with nonorthogonal folding lines (Fig. 1). Those types of unit cells not only require double slicing similar to what was described before for category 2 but also need to be unfolded along nonorthogonal lines (Fig. 1). Because of the complex spatial rotations that are required during the folding process, every other half-floor [B_1, B_2,… (pink) in Fig. 1] should branch out of a main backbone [A_1, A_2,… (green) in Fig. 1] that connects the remaining half-floors to each other in series (Fig. 1 and fig. S3). Lattices based on a number of space-filling polyhedra, such as rhombic dodecahedron, could be folded using this type of folding pattern (Fig. 2A). Videos S1 to S3 show the initially flat state, the folding sequences and the resulting lattice structures for some sample unit cells from each category. Although the three folding patterns presented here cover a large number of space-filling polyhedra, it is not clear how many of the hundreds of space-filling polyhedra (*38*) could be folded using the proposed patterns or slight modifications of those. On the other hand, a number of other (derivative) unit cell geometries could be folded using these patterns.

In the cases where the unfolded (half-)floors (that is, A_1, A_2,…, B_1, B_2,…) are connected in series (that is, category 1 and the main variant of category 2), one could first fold the (half-)floors individually and then fold the entire lattice. In the cases where there is a backbone and half-floors that are branching out from that (that is, category 3 and two variants of category 2), the facing half-floors, which make individual floors, should fold and meet each other first before all floors are folded to create the entire lattice. Therefore, sequential folding is needed in those cases. Even when sequential folding is not essential to fold the lattice (for example, category 1), it could improve the reliability of the folding

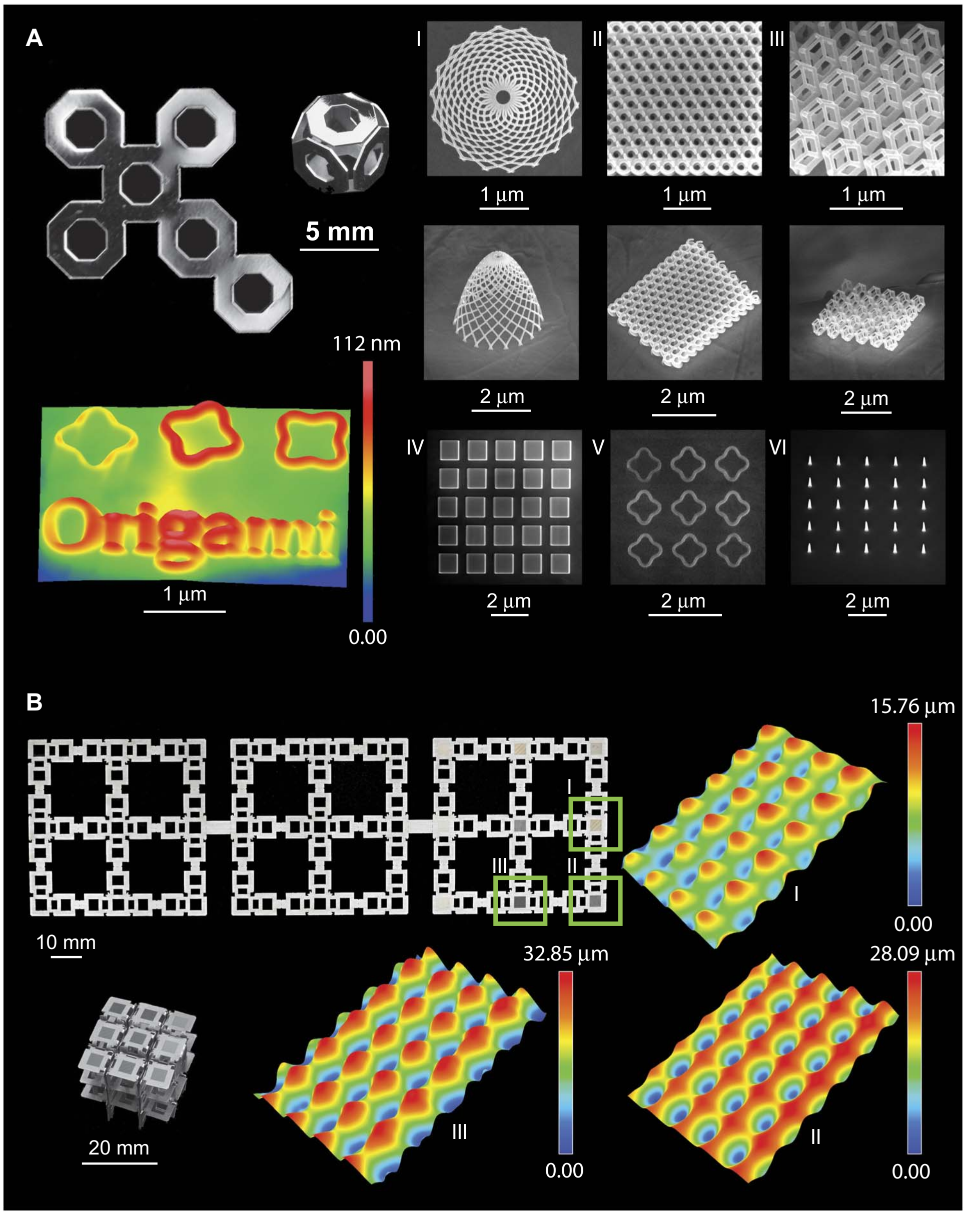

Fig. 4. Free-form ornamentation of origami lattices. (**A**) EBID was used to deposit gasified platinum-based precursor on top of a polished flat origami truncated octahedron cut from a 200-µm pure titanium foil. Multiple 2D and hierarchical 3D patterns have been produced with feature sizes in the range of a few tens of nanometers. The surface ornaments were imaged using scanning electron microscopy (SEM). The dimensions of the ornaments were measured with atomic force microscopy (AFM; details in the Supplementary Materials). (**B**) A flat pure titanium foil was patterned using an ultrashort pulse laser. Three spots in the unfolded sheet were patterned using three different types of pattern design. The final configuration of folded lattice shows the arrangement of the three patterned spots. The profiles of the patterns were measured using 3D optical microscopy (details in the Supplementary Materials).

process by minimizing the chance of interlocking incidents. This is particularly important when locking mechanisms are incorporated in the design of the lattice to increase its structural integrity.

Self- and sequential folding

We also demonstrated the self-folding of lattice structures from initially flat states using 3D-printed thick panels that hinged at the folding lines (Fig. 2). We used simple elastic bands to program sequential folding into the flat assembly of panels. The number of elastic bands determined the amount of stored potential energy, which then converted to kinetic energy and determined the speed of the different segments of the assembly during the folding process. That programmed sequential folding allowed for complete folding of the lattice structure from an initially flat state (see video S4). The designed cubic lattice also incorporated locking mechanisms that, subsequent to self-folding, locked the different segments of the panels into each other and guaranteed the mechanical performance of the folded lattice structure.

Mechanical metamaterials

The topology of the unit cells significantly influences the mechanical properties of lattice structures independent of their relative density (or porosity) (*39*). Therefore, mechanical metamaterials with unusual properties could be designed by changing the topology of the unit cells. Because adjusting the Poisson's ratio is one of the aims of these designs, here we present two types of fully folded mechanical metamaterials with negative (reentrant unit cell) and zero (cubic unit cell) values of the Poisson's ratio (Fig. 3). Locking mechanisms similar to what was shown before were incorporated in the design of the cubic lattice structure (Fig. 3A) to ensure its ability to tolerate mechanical loading. The lattices were manually folded from aluminum sheets and subsequently tested under compression (Fig. 3, C to E). Both lattices showed significant mechanical properties (Fig. 3, C and D). The Poisson's ratio of the auxetic lattice structure (based on the ensemble average of selected reentrant unit cells on the front side of the reentrant lattice) was determined using image processing techniques and was found to significantly change with the applied axial deformation (Fig. 3E). The cubic lattice failed in a layer-by-layer fashion, largely preserving its near-zero Poisson's ratio, whereas the final shape of the reentrant-based lattice structure clearly showed the auxetic behavior of this mechanical metamaterial.

Free-form surface ornamentation

To demonstrate the extent of freedom offered by the proposed approach in terms of surface ornamentation, we used two distinct techniques to decorate the surfaces of origami lattices at both the micro- and nanoscales (Fig. 4). The first technique, that is, EBID, could be considered a 3D printing technique with a theoretical resolution in the "subnanometer" range (*40*). We used EBID (see the Supplementary Materials for the methodological details) not only to create nanopatterns and write on the surface of flat origami sheets but also to create free-form 3D shapes and lattice structures with feature sizes in the range of a few tens of nanometers (Fig. 4A). Combining the surface ornaments that are demonstrated here with the lattice folding patterns, it is possible to create hierarchical lattice structures that also cover the internal surfaces of porous lattices. The second patterning technique, namely, ultrashort pulse laser micromachining, was used to apply patterns at the micrometer scale (Fig. 4B). For both techniques, the type, geometry, and size of the ornaments could be very different from one place within the flat sheet to another. Functionally graded ornaments, that is, ornaments with spatially varying topology and dimensions, could then be realized. For example, we packed multiple types of surface patterns into the same origami lattice (Fig. 4B).

DISCUSSION

There are several areas where the proposed approach could be used for creating metamaterials with advanced functionalities. One specific area is the development of (meta-)biomaterials that stimulate tissue regeneration. Recent studies have shown that very specific nanotopographies could determine stem cell fate and induce cell differentiation toward the preferred lineage (*18*, *24*, *41*). Advanced surface ornamentation techniques such as those presented here are capable of producing the required nanotopographies, but only on flat surfaces. At the same time, highly ordered porous lattice structures with fully interconnected porosities are needed to simultaneously provide mechanical support for tissue regeneration and facilitate the transport of oxygen and nutrients to cells (*42*, *43*). The approach proposed here allows for combining the biofunctionalities offered by surface ornaments with those provided by highly ordered lattice structures and will be pursued in our future research. Another example of the potential areas of application would be the integration of flexible electronics (for example, sensors and actuators) in the design of (mechanical) metamaterials.

CONCLUSIONS

Here, the approach presented for fabrication of lattice structures with internal surfaces that are covered with arbitrarily complex ornaments is unprecedented, general, and scalable. Different variants of this approach with alternative folding patterns, self-folding techniques, and surface ornamentation methods could be used to suit the needs of various application areas. Using other surface ornamentation techniques such as optical and electron beam lithography and combining the current techniques with techniques such as nanoimprinting could maximize the scalability of the ornamentation techniques.

MATERIALS AND METHODS

The polymeric models of (self-folding) lattice structures (Fig. 2 and fig. S4) were fabricated with a 3D printer (Ultimaker 2+; Ultimaker, Netherlands) working based on fused deposition modeling and using polylactic acid filaments (diameter, 2.85 mm; Ultimaker). Prestretched elastic bands were used as active elements. Sequential folding was achieved by adjusting the number of the prestretched elastic bands.

The metallic lattices (Fig. 3) were folded from an aluminum sheet (1050A with a nominal elastic modulus of 71 GPa) and a thickness of 0.8 mm, which was laser-cut to create the unfolded state of a cubic structure comprising three unit cells in each direction (see Fig. 3 and fig. S5 for details). To fixate the top and bottom floors during mechanical testing, a polymethyl methacrylate plate (thickness, 8 mm) was laser-cut to create matching grooves that accommodated the free ends of the lattice structure. The same type of sheet (thickness, 0.5 mm) was laser-cut and folded to form the different floors of the reentrant lattice (Fig. 3), which were later mounted on top of each other to create the full lattice structure. Clamps with matching grooves were 3D-printed using an Ultimaker 2+ printer (Ultimaker) and polylactic acid filaments (diameter, 2.85 mm; Ultimaker). The folded floors (together with their clamps; fig. S5) were placed under 2 kg of compressive load for 15 min to minimize the springback of the folds. The floors were then assembled using double-sided tapes (polyester tape type FT 4967, Tesa) and were put under compressive preload similar to what was explained for the folded floors. The folded lattices were then compressed uniaxially using a Lloyd LR5K mechanical testing machine equipped with a 5-kN load cell. A high-resolution digital camera (Sony A7R with a Sony FE 90-mm f/2.8 macro OSS lens) was used to record the trend of the deformations. A group of unit cells (five full unit cells and two halves) in the middle of the front side of the reentrant lattice were selected to estimate the evolution in the Poisson's ratio as the compressive strain increased.

To create the nanopattern using the EBID technique (Fig. 4A), a truncated cube origami unit cell was first laser-cut and manually polished using 3- and 1-μm water-based diamond suspensions for 30 min. The final polish was performed with colloidal silica suspension (OP-S, Struers) and an automatic polisher (RotoPol-31 and RotoForce-4, Struers) for 20 min, giving a roughness of 5 ± 3 nm based on four selected squares of 1.5 × 1.5 μm. Prior to patterning, the samples were cleaned ultrasonically in acetone for 5 min, soaked in isopropanol, and then dried with compressed nitrogen gas and in the oven at 90°C. By using trimethyl(methylcyclopentadienyl)-platinum (IV) ($MeCpPtMe_3$) precursor in a Nova NanoLab 650 DualBeam system (FEI), various shapes, from simple arrays of squares and pillars to complex 3D shapes, were generated at different locations within the polished surface of the titanium unit cell.

For laser patterning (Fig. 4B), a smaller version of the cubic lattice used for mechanical testing was laser-cut from a pure titanium foil (thickness, 0.125 mm; purity, 99.6+%, annealed; Goodfellow). Nine different surface patterns were created in nine different spots of the top floor of the cubic lattice using laser micromachining (machine: 3D Micromac, PicoBlade laser; wavelength, 355 nm; scanner, 163 mm; Lumentum, performed by Reith Laser, Netherlands). The samples were then carefully washed and dried. A digital optical microscope (VHX-5000; Keyence) was used to produce the 3D images of resulting patterns by merging multiple images taken at varying depths of focus (Fig. 4B).

Following EBID, the generated surface ornaments were directly inspected with SEM and images were acquired at various magnifications both under horizontal and tilted positions. Selected structures were also imaged with AFM using a FastScan-A probe (Bruker) with a tip radius of 5 nm and nominal spring constants of 18 N/m. Experiments were conducted under ambient conditions. ScanAsyst mode was implemented with a scan rate of 3.91 Hz. ScanAsyst (Bruker) is a tapping-based mode with automatic image optimization. The results obtained from AFM were then analyzed using Gwyddion 2.47.

SUPPLEMENTARY MATERIALS

Supplementary material for this article is available at http://advances.sciencemag.org/cgi/content/full/3/11/eaao1595/DC1

section S1. Design and folding sequence
section S2. Self-folding lattices
section S3. Folded mechanical metamaterials
section S4. Free-form surface ornamentation
fig. S1. Illustration of thick panel cubic lattice origami (category 1).
fig. S2. The serial connection of three half-floors in a truncated octahedron lattice (category 2).
fig. S3. A category 3 lattice made from the rhombic dodecahedron unit cell.
fig. S4. Arrangement of joints in hinged panels.
fig. S5. Fully folded cubic and reentrant lattices.
fig. S6. The initial configuration of the ensemble determined from the recorded images using the developed MATLAB code.
fig. S7. Schematic drawing of the EBID process.
fig. S8. Position of the titanium sample inside the EBID microscope chamber.
fig. S9. SEM images of the EBID structures produced on the titanium unit cell.
fig. S10. Selected AFM images of EBID structures with representative line profiles used to quantify the characteristic dimensions of the EBID structures.
table S1. EBID process conditions.
table S2. Characteristic dimensions of the EBID structures, as determined from the AFM, SEM, and stream files.
video S1. The kinematics of self-folding in cubic lattice origami.
video S2. The kinematics of self-folding in truncated octahedron lattice origami.
video S3. Sequential folding of rhombic dodecahedron lattice origami.
video S4. Sequential folding of cubic lattice prototype.
References (*44*–*54*)

REFERENCES AND NOTES

1. J. Valentine, S. Zhang, T. Zentgraf, E. Ulin-Avila, D. A. Genov, G. Bartal, X. Zhang, Three-dimensional optical metamaterial with a negative refractive index. *Nature* **455**, 376–379 (2008).
2. V. M. Shalaev, Optical negative-index metamaterials. *Nat. Photonics* **1**, 41–48 (2007).
3. I. M. Pryce, K. Aydin, Y. A. Kelaita, R. M. Briggs, H. A. Atwater, Highly strained compliant optical metamaterials with large frequency tunability. *Nano Lett.* **10**, 4222–4227 (2010).
4. D. Schurig, J. J. Mock, B. J. Justice, S. A. Cummer, J. B. Pendry, A. F. Starr, D. R. Smith, Metamaterial electromagnetic cloak at microwave frequencies. *Science* **314**, 977–980 (2006).
5. S. Zhang, C. Xia, N. Fang, Broadband acoustic cloak for ultrasound waves. *Phys. Rev. Lett.* **106**, 024301 (2011).
6. A. A. Zadpoor, Mechanical meta-materials. *Mater. Horiz.* **3**, 371–381 (2016).
7. X. Zheng, H. Lee, T. H. Weisgraber, M. Shusteff, J. DeOtte, E. B. Duoss, J. D. Kuntz, M. M. Biener, Q. Ge, J. A. Jackson, S. O. Kucheyev, N. X. Fang, C. M. Spadaccini, Ultralight, ultrastiff mechanical metamaterials. *Science* **344**, 1373–1377 (2014).
8. M. Kadic, T. Bückmann, N. Stenger, M. Thiel, M. Wegener, On the practicability of pentamode mechanical metamaterials. *Appl. Phys. Lett.* **100**, 191901 (2012).
9. J.-H. Lee, L. Wang, M. C. Boyce, E. L. Thomas, Periodic bicontinuous composites for high specific energy absorption. *Nano Lett.* **12**, 4392–4396 (2012).
10. K. E. Evans, A. Alderson, Auxetic materials: Functional materials and structures from lateral thinking! *Adv. Mater.* **12**, 617–628 (2000).
11. Q. Wang, J. A. Jackson, Q. Ge, J. B. Hopkins, C. M. Spadaccini, N. X. Fang, Lightweight mechanical metamaterials with tunable negative thermal expansion. *Phys. Rev. Lett.* **117**, 175901 (2016).
12. Y. Chen, S. Zhou, Q. Li, Microstructure design of biodegradable scaffold and its effect on tissue regeneration. *Biomaterials* **32**, 5003–5014 (2011).
13. X. Sun, Y. Kang, J. Bao, Y. Zhang, Y. Yang, X. Zhou, Modeling vascularized bone regeneration within a porous biodegradable CaP scaffold loaded with growth factors. *Biomaterials* **34**, 4971–4981 (2013).
14. M. Vaezi, H. Seitz, S. Yang, A review on 3D micro-additive manufacturing technologies. *Int. J. Adv. Des. Manuf. Techol.* **67**, 1721–1754 (2013).
15. M. Lee, H.-Y. Kim, Toward nanoscale three-dimensional printing: Nanowalls built of electrospun nanofibers. *Langmuir* **30**, 1210–1214 (2014).
16. M. Röhrig, M. Thiel, M. Worgull, H. Hölscher, 3D direct laser writing of nano- and microstructured hierarchical gecko-mimicking surfaces. *Small* **8**, 3009–3015 (2012).
17. J. Bauer, A. Schroer, R. Schwaiger, O. Kraft, Approaching theoretical strength in glassy carbon nanolattices. *Nat. Mater.* **15**, 438–443 (2016).
18. M. J. Dalby, N. Gadegaard, R. Tare, A. Andar, M. O. Riehle, P. Herzyk, C. D. W. Wilkinson, R. O. C. Oreffo, The control of human mesenchymal cell differentiation using nanoscale symmetry and disorder. *Nat. Mater.* **6**, 997–1003 (2007).
19. J. Fu, Y.-K. Wang, M. T. Yang, R. A. Desai, X. Yu, Z. Liu, C. S. Chen, Mechanical regulation of cell function with geometrically modulated elastomeric substrates. *Nat. Methods* **7**, 733–736 (2010).
20. H. N. Kim, A. Jiao, N. S. Hwang, M. S. Kim, D. H. Kang, D.-H. Kim, K.-Y. Suh, Nanotopography-guided tissue engineering and regenerative medicine. *Adv. Drug Deliv. Rev.* **65**, 536–558 (2013).
21. J. Shi, A. R. Votruba, O. C. Farokhzad, R. Langer, Nanotechnology in drug delivery and tissue engineering: From discovery to applications. *Nano Lett.* **10**, 3223–3230 (2010).
22. M. M. Stevens, Biomaterials for bone tissue engineering. *Mater. Today* **11**, 18–25 (2008).
23. E. K. F. Yim, E. M. Darling, K. Kulangara, F. Guilak, K. W. Leong, Nanotopography-induced changes in focal adhesions, cytoskeletal organization, and mechanical properties of human mesenchymal stem cells. *Biomaterials* **31**, 1299–1306 (2010).
24. M. J. Dalby, N. Gadegaard, R. O. C. Oreffo, Harnessing nanotopography and integrin–matrix interactions to influence stem cell fate. *Nat. Mater.* **13**, 558–569 (2014).
25. T. Sun, L. Feng, X. Gao, L. Jiang, Bioinspired surfaces with special wettability. *Acc. Chem. Res.* **38**, 644–652 (2005).
26. T. L. Liu, C.-J. Kim, Turning a surface superrepellent even to completely wetting liquids. *Science* **346**, 1096–1100 (2014).
27. E. Martines, K. Seunarine, H. Morgan, N. Gadegaard, C. D. W. Wilkinson, M. O. Riehle, Superhydrophobicity and superhydrophilicity of regular nanopatterns. *Nano Lett.* **5**, 2097–2103 (2005).
28. A. Rahman, A. Ashraf, H. Xin, X. Tong, P. Sutter, M. D. Eisaman, C. T. Black, Sub-50-nm self-assembled nanotextures for enhanced broadband antireflection in silicon solar cells. *Nat. Commun.* **6**, 5963 (2015).
29. L. Zhao, S. Mei, P. K. Chu, Y. Zhang, Z. Wu, The influence of hierarchical hybrid micro/nano-textured titanium surface with titania nanotubes on osteoblast functions. *Biomaterials* **31**, 5072–5082 (2010).
30. S. Kim, U. T. Jung, S.-K. Kim, J.-H. Lee, H. S. Choi, C.-S. Kim, M. Y. Jeong, Nanostructured multifunctional surface with antireflective and antimicrobial characteristics. *ACS Appl. Mater. Interfaces* **7**, 326–331 (2015).
31. S. Kim, B. Marelli, M. A. Brenckle, A. N. Mitropoulos, E.-S. Gil, K. Tsioris, H. Tao, D. L. Kaplan, F. G. Omenetto, All-water-based electron-beam lithography using silk as a resist. *Nat. Nanotechnol.* **9**, 306–310 (2014).
32. H. Schift, Nanoimprint lithography: An old story in modern times? A review. *J. Vac. Sci. Technol., B* **26**, 458 (2008).
33. Z. Nie, E. Kumacheva, Patterning surfaces with functional polymers. *Nat. Mater.* **7**, 277–290 (2008).
34. S. W. Lee, B.-K. Oh, R. G. Sanedrin, K. Salaita, T. Fujigaya, C. A. Mirkin, Biologically active protein nanoarrays generated using parallel dip-pen nanolithography. *Adv. Mater.* **18**, 1133–1136 (2006).
35. R. Steve, P. Robert, A review of focused ion beam applications in microsystem technology. *J. Micromech. Microeng.* **11**, 287 (2001).
36. W. F. van Dorp, C. W. Hagen, A critical literature review of focused electron beam induced deposition. *J. Appl. Phys.* **104**, 081301 (2008).
37. E. D. Demaine, M. L. Demaine, J. S. B. Mitchell, Folding flat silhouettes and wrapping polyhedral packages: New results in computational origami. *Comput. Geom.* **16**, 3–21 (2000).

38. D. G. Wells, *The Penguin Dictionary of Curious and Interesting Geometry* (Penguin Books, 1991).
39. A. A. Zadpoor, R. Hedayati, Analytical relationships for prediction of the mechanical properties of additively manufactured porous biomaterials. *J. Biomed. Mater. Res. A* **104**, 3164–3174 (2016).
40. W. F. van Dorp, B. van Someren, C. W. Hagen, P. Kruit, P. A. Crozier, Approaching the resolution limit of nanometer-scale electron beam-induced deposition. *Nano Lett.* **5**, 1303–1307 (2005).
41. S. Dobbenga, L. E. Fratila-Apachitei, A. A. Zadpoor, Nanopattern-induced osteogenic differentiation of stem cells—A systematic review. *Acta Biomater.* **46**, 3–14 (2016).
42. S. J. Hollister, Porous scaffold design for tissue engineering. *Nat. Mater.* **4**, 518–524 (2005).
43. F. S. L. Bobbert, A. A. Zadpoor, Effects of bone substitute architecture and surface properties on cell response, angiogenesis, and structure of new bone. *J. Mater. Chem. B* **5**, 6175–6192 (2017).
44. I. Utke, H. W. P. Koops, The historical development of electron beam induced deposition and etching: from carbon to functional materials. in *Nanofabrication using Focused Ion and Electron Beams: Principles and Applications*, I. Utke, S. Moshkalev, P. Russel, Eds. (Oxford Univ. Press, 2012), pp. 3–35.
45. A. Fernandez-Pacheco, L. Serrano-Ramón, J. M. Michalik, M. R. Ibarra, J. M. De Teresa, L. O'Brien, D. Petit, J. Lee, R. P. Cowburn, Three dimensional magnetic nanowires grown by focused electron-beam induced deposition. *Sci. Rep.* **3**, 1492 (2013).
46. J. M. De Teresa, A. Fernández-Pacheco, R. Córdoba, L. Serrano-Ramón, S. Sangiao, M. R. Ibarra, Review of magnetic nanostructures grown by focused electron beam induced deposition (FEBID). *J. Phys. D Appl. Phys.* **49**, 243003 (2016).
47. P. Peinado, S. Sangiao, J. M. De Teresa, Focused electron and ion beam induced deposition on flexible and transparent polycarbonate substrates. *ACS Nano* **9**, 6139–6146 (2015).
48. C. Shi, D. K. Luu, Q. Yang, J. Liu, J. Chen, C. Ru, S. Xie, J. Luo, J. Ge, Y. Sun, Recent advances in nanorobotic manipulation inside scanning electron microscopes. *Microsyst. Nanoeng* **2**, 16024 (2016).
49. J. D. Beard, S. N. Gordeev, Fabrication and buckling dynamics of nanoneedle AFM probes. *Nanotechnology* **22**, 175303 (2011).
50. A. P. Ivanov, E. Instuli, C. M. McGilvery, G. Baldwin, D. W. McComb, T. Albrecht, J. B. Edel, DNA tunneling detector embedded in a nanopore. *Nano Lett.* **11**, 279–285 (2011).
51. P. C. Post, A. Mohammadi-Gheidari, C. W. Hagen, P. Kruit, Parallel electron-beam-induced deposition using a multi-beam scanning electron microscope. *J. Vac. Sci. Technol. B Microelectron. Nanometer Struct. Process Meas. Phenom.* **29**, 06F310 (2011).
52. M. Scotuzzi, M. J. Kamerbeek, A. Goodyear, M. Cooke, C. W. Hagen, Pattern transfer into silicon using sub-10 nm masks made by electron beam-induced deposition. *J. Micro Nanolithogr. MEMS MOEMS* **14**, 031206 (2015).
53. A. V. Riazanova, B. N. Costanzi, A. I. Aristov, Y. G. M. Rikers, J. J. L. Mulders, A. V. Kabashin, E. Dan Dahlberg, L. M. Belova, Gas-assisted electron-beam-induced nanopatterning of high-quality titanium oxide. *Nanotechnology* **27**, 115304 (2016).
54. C. W. Hagen, The future of focused electron beam-induced processing. *Appl. Phys. A* **117**, 1599–1605 (2014).

Funding: The research leading to these results has received funding from the European Research Council (ERC) under the ERC grant agreement no. 677575. **Author contributions:** S.J. and A.A.Z. conceived the study. S.J. designed the lattices and produced the prototypes. N.N. and D.S.W. produced the 3D and 2D nanostructures. S.J. and A.A.Z. wrote the manuscript. C.W.H., L.E.F.-A., and A.A.Z. supervised the project. All authors contributed to the analysis of the results, the reading and editing of the manuscript, and the approval of the final version. **Competing interest:** The authors declare that they have no competing interest. **Data and materials availability:** All data needed to evaluate the conclusions in the paper are present in the paper and/or the Supplementary Materials. Additional data related to this paper may be requested from the authors.

Submitted 20 June 2017
Accepted 6 November 2017
Published 29 November 2017
10.1126/sciadv.aao1595

Citation: S. Janbaz, N. Noordzij, D. S. Widyaratih, C. W. Hagen, L. E. Fratila-Apachitei, A. A. Zadpoor, Origami lattices with free-form surface ornaments. *Sci. Adv.* **3**, eaao1595 (2017).

Science Advances

Origami lattices with free-form surface ornaments

Shahram Janbaz, Niels Noordzij, Dwisetya S. Widyaratih, Cornelis W. Hagen, Lidy E. Fratila-Apachitei and Amir A. Zadpoor

Sci Adv **3** (11), eaao1595.
DOI: 10.1126/sciadv.aao1595